Physics in Medicine & Biology

IPEM Institute of Physics and Engineering in Medicine

PAPER

Parameter estimation using macroscopic diffusion MRI signal models

To cite this article: Hang Tuan Nguyen *et al* 2015 *Phys. Med. Biol.* **60** 3389

View the article online for updates and enhancements.

Related content

- Numerical simulation of diffusion MRI signals using an adaptive time-stepping method
  Jing-Rebecca Li, Donna Calhoun, Cyril Poupon et al.
- Measuring diffusion and perfusion using MRI
  David L Thomas, Mark F Lythgoe, Gaby S Pell et al.
- Simulations on the influence of myelin water in diffusion-weighted imaging
  K D Harkins and M D Does

Recent citations

- Quantifying brain microstructure with diffusion MRI: Theory and parameter estimation
  Dmitry S. Novikov *et al*
- The Kärger vs bi-exponential model: theoretical insights and experimental validations
  Nicolas Moutal *et al*

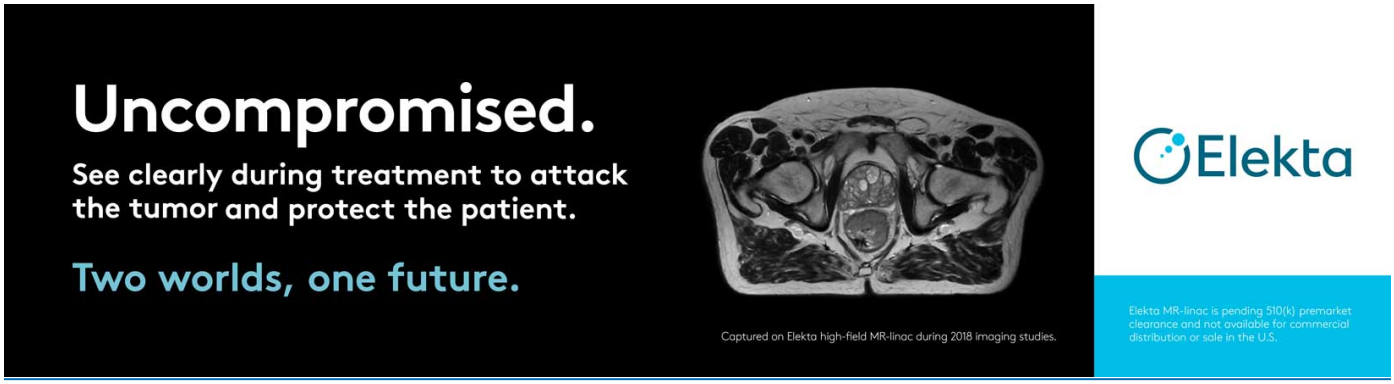

This content was downloaded from IP address 128.93.162.219 on 27/02/2019 at 07:52

IOP Publishing | Institute of Physics and Engineering in Medicine Physics in Medicine & Biology

Phys. Med. Biol. **60** (2015) 3389–3413 doi:10.1088/0031-9155/60/8/3389

Parameter estimation using macroscopic diffusion MRI signal models

Hang Tuan Nguyen[3], Denis Grebenkov[2], Dang Van Nguyen[1,3], Cyril Poupon[3], Denis Le Bihan[3] and Jing-Rebecca Li[1,3]

[1] INRIA Saclay-Equipe DEFI, CMAP, Ecole Polytechnique Route de Saclay, 91128, Palaiseau Cedex, France
[2] Laboratoire de Physique de la Matière Condensée, CNRS—Ecole Polytechnique, F-91128 Palaiseau Cedex, France
[3] NeuroSpin, CEA Saclay Center, 91191 Gif-sur-Yvette Cedex, France

E-mail: jingrebecca.li@inria.fr

Received 7 July 2014, revised 5 January 2015
Accepted for publication 22 January 2015
Published 2 April 2015

Abstract

Macroscopic models of the diffusion MRI (dMRI) signal can be helpful to understanding the relationship between the tissue microstructure and the dMRI signal. We study the least squares problem associated with estimating tissue parameters such as the cellular volume fraction, the residence times and the effective diffusion coefficients using a recently developed macroscopic model of the dMRI signal called the Finite Pulse Kärger model that generalizes the original Kärger model to non-narrow gradient pulses. In order to analyze the quality of the estimation in a controlled way, we generated synthetic noisy dMRI signals by including the effect of noise on the exact signal produced by the Finite Pulse Kärger model. The noisy signals were then fitted using the macroscopic model. Minimizing the least squares, we estimated the model parameters. The bias and standard deviations of the estimated model parameters as a function of the signal to noise ratio (SNR) were obtained. We discuss the choice of the *b*-values, the least square weights, the extension to experimentally obtained dMRI data as well noise correction.

Keywords: diffusion MRI, macroscopic model, parameter estimation

(Some figures may appear in colour only in the online journal)

1. Introduction

In diffusion magnetic resonance imaging (dMRI), water motion inside a biological tissue is monitored in order to characterize the tissue microstructure. Varying magnetic field gradients

and diffusion times, one acquires the macroscopic signal (at millimeter spatial resolution) which aggregates statistically averaged information about the domain at the micrometer scale. Inferring the microstructure from the macroscopic signal is a formidable inverse problem (Grebenkov 2007).

The complexity of brain tissue does not allow the extraction of the whole microstructure. Rather, one focuses on estimating some macroscopic parameters of the tissue whose changes can be related to physiological or pathological modifications. In the diffusion tensor model (Basser *et al* 1994) water diffusion was modeled as a Gaussian process whereas the diffusion kurtosis model (Chabert *et al* 2005, Jensen *et al* 2005) included additional degrees of freedom for a better fit of the dMRI signal. The dMRI signal has been also modeled as the sum of two or multiple decaying exponentials, representing, for example, fast and slow Gaussian diffusion pools. Although the explicit form of this representation makes the bi-exponential model very attractive, naive identifications of the extracted volume fractions of the pools as volume fractions of the physiological constituents of the tissue, i.e. the cells (slow diffusion) and the extracellular space (fast diffusion), have failed (Niendorf *et al* 1996, Mulkern *et al* 1999, Clark and Le Bihan 2000, Chin *et al* 2002, Lee and Springer 2003, Stanisz 2003, Schwarcz *et al* 2004, Ababneh *et al* 2005). There also have been macroscopic models that explicitly use certain biological quantities as model parameters. For example, if the neurites are modeled by cylinders, while the extracellular space as a Gaussian pool, the total dMRI signal can be represented as the sum of the two explicitly known signals from both compartments (Sen and Basser 2005, Jespersen *et al* 2007, Assaf *et al* 2008). The radius of neurites appears here as a parameter of the model. Note that this explicit representation relies on the Gaussian phase approximation (Grebenkov 2007) and assumes no water exchange between the compartments.

The Kärger model (Kärger *et al* 1988) allows for water exchange between effective Gaussian compartments and incorporates macroscopic parameters such as the cellular volume fraction, the residence times, as well as the effective diffusion coefficients. When the gradient pulses are narrow (as compared to diffusion time), the time evolution of the signals in the different compartments can be described by a system of coupled ordinary differential equations (ODEs). The ODE system can be solved analytically, yielding an explicit dependence of the dMRI signal on the model parameters. This explicit representation of the dMRI signal can then be used to estimate the residence times and the volume fractions of water molecules in the effective Gaussian diffusion pools. Fieremans *et al.* proposed a coarse graining argument to justify the concept of co-existing pools of water molecules and validated the Kärger model by Monte Carlo simulations (Fieremans *et al* 2010) (see also Meier *et al* (2003) and Nilsson *et al* (2010) for Monte Carlo simulations). In particular, the slow exchange between compartments (i.e. low permeability) was shown to be necessary for compartment separation. In spite of these limitations, the Kärger model has been often used in biological tissue imaging to invert for model parameters (Stanisz *et al* 1997, Waldeck *et al* 1997, Pfeuffer *et al* 1998, Lee and Springer 2003, Meier *et al* 2003, Quirk *et al* 2003, Roth *et al* 2008, Aslund *et al* 2009, Nilsson *et al* 2009).

Recently, a new macroscopic model for the dMRI signal was formulated (Coatléven *et al* 2014, Li *et al* 2014) using homogenization techniques (Bensoussan *et al* 1978). The compartments of this macroscopic model are the biological cells and the extracellular space that are separated from each other by cell membranes. By matching asymptotic expansions of the solution of the microscopic Bloch–Torrey partial differential equation (PDE) in different compartments, the dMRI signal is given as the solution of a system of coupled ODEs. These ODEs are similar to that of the Kärger model, but they have time-dependent coefficients so that the solution is obtained numerically. As the main advantage, this new macroscopic model is not subject to the narrow pulse restriction, in contrast to the Kärger model. The gradient pulses

can be long in duration and can have an arbitrary temporal profile. The work of (Coatléven *et al* 2014) can be thought of as giving a sound mathematical basis to the Kärger model as well as generalizing it beyond narrow gradient pulses.

In this paper, we consider the weighted least squares problem associated with estimating the macroscopic model parameters such as the cellular volume fraction, the residence times and the effective diffusion coefficients using the Finite Pulse Kärger (FPK) model. There have been many works on estimating the parameters of the diffusion tensor and the diffusion kurtosis models in the presence of noise and noise correction. See Veraart *et al* (2013a, 2013b), Collier *et al* (2014), Iima *et al* (2015) and Veraart *et al* (2011) and references therein. The major difference between the diffusion tensor or kurtosis models and the FPK model that we consider in this paper is that the data cannot be easily represented as a linear function of the model parameters (as it was done, e.g. in the diffusion tensor model by taking the logarithm of the signal). In other words, one has to deal with nonlinear fitting so that the parameters estimation becomes much more involved.

To proceed with our study, we first solve the Bloch–Torrey equation for the complex transverse magnetization on a geometry containing spherical cells of various sizes to show that the total complex transverse magnetization is accurately represented by the solution of the FPK model over an appropriate range of b-values. In this way, the FPK model is identified as an appropriate macroscopic fitting frame for this geometrical example. We then investigate in depth the robustness of parameters estimation within this model. Following the standard scheme, we first simulate the dMRI signal within the FPK model with prescribed parameters, add noise and then fit the noisy signal to the FPK model by minimizing the least squares in order to estimate the model parameters. The quality of the estimation procedure can be accessed by comparing the estimated parameters to their true values. The bias and standard deviations of the estimated model parameters as a function of the signal to noise ratio (SNR) were obtained. We discuss the choice of the b-values, the least square weights, the extension to experimentally obtained dMRI data as well noise correction.

2. Theory

To validate the FPK model, we define a simplified geometrical model of a biological tissue in a computational box $C = [-L_1/2, L_1/2] \times [-L_2/2, L_2/2] \times [-L_3/2, L_3/2]$ and assume that C is periodically repeated in all three dimensions to make up the imaging voxel. Inside C, there are sphere compartments, Ω^j, $j = 2, \cdots$ (where each Ω^j is a sphere), while the remaining set $\Omega^1 = C \backslash \cup_{j \geqslant 2} \Omega^j$ is called the extracellular compartment.

2.1. Microscopic Bloch–Torrey equation

A 'ground truth' dMRI signal can be computed by solving the multiple compartment Bloch–Torrey PDE in C (Torrey 1956, Grebenkov 2010)

$$\frac{\partial M^l(\mathbf{r}, t \mid \mathbf{g})}{\partial t} = -\mathrm{i} f(t)(\gamma \mathbf{g} \cdot \mathbf{r}) M^l(\mathbf{r}, t \mid \mathbf{g}) + \nabla \cdot (D^0 \nabla M^l(\mathbf{r}, t \mid \mathbf{g})) \quad (\mathbf{r} \in \Omega^l), \tag{1}$$

where $M^l(\mathbf{r}, t \mid \mathbf{g})$ is the complex-valued transverse water proton magnetization at $\mathbf{r} = (r_1, r_2, r_3)$ in compartment Ω^l, $\mathbf{g} = (g_1, g_2, g_3)$ is the diffusion-encoding gradient, $f(t)$ is its effective temporal profile, i is the imaginary unit, $\gamma = 2.675 \cdot 10^8$ rad/s/Tesla is the gyromagnetic ratio of the water proton and D^0 is the intrinsic diffusion coefficient of water molecules. The PDEs in equation (1) are supplemented with two interface conditions on the interface Γ^{ln} between

any two adjacent compartments Ω^l and Ω^n. One interface condition is the continuity of magnetization flux:

$$D^0(\nabla M^l(\mathbf{r}, t \mid \mathbf{g}) \cdot \mathbf{n}^l(\mathbf{r})) = -D^0(\nabla M^n(\mathbf{r}, t \mid \mathbf{g}) \cdot \mathbf{n}^n(\mathbf{r})), \quad \mathbf{r} \in \Gamma^{ln}, \tag{2}$$

where $\mathbf{n}^l(\mathbf{r})$ and $\mathbf{n}^n(\mathbf{r})$ are the *outward*-pointing normals to Ω^l and Ω^n at $\mathbf{r}$. The second interface condition,

$$D^0(\nabla M^l(\mathbf{r}, t|\mathbf{g}) \cdot \mathbf{n}^l(\mathbf{r})) = \kappa(M^n(\mathbf{r}, t|\mathbf{g}) - M^l(\mathbf{r}, t|\mathbf{g})), \quad \mathbf{r} \in \Gamma^{ln}, \tag{3}$$

incorporates a permeability κ across Γ^{ln} and models the ease with which water crosses the interface. The larger the κ, the easier the passage of water. We add the initial condition:

$$M^l(\mathbf{r}, 0 \mid \mathbf{g}) = M_0, \quad \mathbf{r} \in \Omega^l, \quad \forall\ l, \tag{4}$$

where the uniform excitation of the nuclei over the whole voxel is assumed, with M_0 being the initial magnetization.

Since the computational box $C = [-L_1/2, L_1/2] \times [-L_2/2, L_2/2] \times [-L_3/2, L_3/2]$ is periodically repeated, we add the boundary conditions on ∂C following (Xu *et al* 2007):

$$M(\mathbf{r}, t \mid \mathbf{g})|_{r_k=-L_k/2} = M(\mathbf{r}, t \mid \mathbf{g})|_{r_k=L_k/2} e^{i\theta_k(t)}, \quad k = 1, 2, 3, \tag{5}$$

$$\left.\frac{\partial M(\mathbf{r}, t \mid \mathbf{g})}{\partial r_k}\right|_{r_k=-L_k/2} = \left.\frac{\partial M(\mathbf{r}, t \mid \mathbf{g})}{\partial r_k}\right|_{r_k=L_k/2} e^{i\theta_k(t)}, \quad k = 1, 2, 3, \tag{6}$$

for each of the faces perpendicular to the three coordinate axes, where $\theta_k(t) = \gamma\ g_k\ L_k \int_0^t f(s)\,\mathrm{d}s$.

Now we define the compartment magnetization as the integral of the magnetization in Ω^l:

$$\overline{M}^l_{\mathrm{PDE}}(b, t) := \int_{\mathbf{r}\in\Omega^l} M^l(\mathbf{r}, t \mid \mathbf{g})\ \mathrm{d}\mathbf{r}, \quad 0 \le t \le \mathrm{TE}, \tag{7}$$

where TE is the echo time at which the dMRI signal is acquired and the b-value is defined as:

$$b(\mathbf{g}) = \gamma^2 \parallel \mathbf{g} \parallel^2 \int_0^{\mathrm{TE}} \mathrm{d}u \left(\int_0^u f(s)\mathrm{d}s \right)^2. \tag{8}$$

The dMRI signal measured in experiments (without the imaging gradients and T_2 effects) corresponds to

$$S_{\mathrm{PDE}}(b) := \sum_{l=1}^{P} \overline{M}^l_{\mathrm{PDE}}(b, \mathrm{TE}) = \sum_{l=1}^{P} \int_{\mathbf{r}\in\Omega^l} M^l(\mathbf{r}, \mathrm{TE} \mid \mathbf{g})\ \mathrm{d}\mathbf{r}, \tag{9}$$

where P is the number of compartments. Because the computational box C is periodically repeated, $S_{\mathrm{PDE}}(b)$ provides the dMRI signal in the whole voxel.

In a dMRI experiment, the TE and sequence $f(t)$ are usually fixed while $\mathbf{g}$ is varied in amplitude and/or in direction to obtain the signal at different b-values. In the rest of the paper, we will set the initial magnetization to $M_0 = \dfrac{1}{|C|}$, so that $S_{\mathrm{PDE}}(b = 0) = 1$ and $\overline{M}^l_{\mathrm{PDE}}(b, t = 0) = \dfrac{|\Omega^l|}{|C|} := v^l$, where $|\Omega^l|$ is the volume of Ω^l, $|C|$ is the volume of the computational box and v^l is the volume *fraction* of Ω^l.

A standard pulsed-gradient spin-echo (PGSE) sequence is composed of two rectangular gradient pulses of duration δ separated by diffusion time Δ:

$$f(t)=\begin{cases}1 & t_s<t<t_s+\delta,\\ -1 & t_s+\Delta<t<t_s+\Delta+\delta,\\ 0 & \text{otherwise,}\end{cases} \tag{10}$$

where t_s is the start of the first pulse (we set $t_s = 0$ throughout the paper). Although both gradient pulses are of the same polarity in a usual spin-echo sequence, the second gradient pulse is effectively inverted (i.e. $f(t) = -1$) by the refocusing 180° rf pulse. The b-value from equation (8) becomes

$$b = \gamma^2 \parallel \mathbf{g} \parallel^2 \delta^2(\Delta - \delta/3). \tag{11}$$

2.2. Macroscopic Kärger model

The Kärger model (Kärger *et al* 1988) is formulated under the narrow pulse approximation, $\delta \ll \Delta$, for which the compartment magnetizations $\overline{M}^l_{\mathrm{KAR}}(b,t)$, $l = 1, \cdots, P$ satisfy

$$\begin{aligned}\frac{\mathrm{d}\overline{M}^m_{\mathrm{KAR}}(b,t)}{\mathrm{d}t} &= -\left(\delta^2\gamma^2\mathbf{g}^T\overline{D}^m\mathbf{g} + \sum_{l=1,\, l\neq m}^{P}\frac{1}{\tau^{lm}}\right)\overline{M}^m_{\mathrm{KAR}}(b,t)\\ &\quad + \sum_{l=1,\, l\neq m}^{P}\frac{1}{\tau^{ml}}\overline{M}^l_{\mathrm{KAR}}(b,t), \quad m = 1, \cdots, P,\end{aligned} \tag{12}$$

where $\overline{D}^m$ is the *effective* diffusion tensor in compartment m and $1/\tau^{lm}$ is the transfer rate from m-th compartment to l-th compartment. Note that in the case of two compartments, τ^{12} can be interpreted as the residence time in the first (extracellular) compartment. The volume fractions v^l are normalized as

$$\sum_{l=1}^{P} v^l = 1. \tag{13}$$

These coupled ODEs are subject to the initial conditions:

$$\overline{M}^l_{\mathrm{KAR}}(b,0) = v^l, \quad l = 1, \cdots, P. \tag{14}$$

While the dMRI signal is the sum of the $\overline{M}^l_{\mathrm{KAR}}$ from all the compartments at $t = \Delta$:

$$\sum_{l=1}^{P}\overline{M}^l_{\mathrm{KAR}}(b,\Delta),$$

we found that the Kärger model can be made more accurate when the signal is evaluated at $t = \Delta - \delta/3$, similar to the appearance of the factor $\Delta - \delta/3$ in the b-value in equation (11). Thus, we will use the expression

$$S_{\mathrm{KAR}}(b) = \sum_{l=1}^{P}\overline{M}^l_{\mathrm{KAR}}(b,\Delta-\delta/3)$$

for the dMRI signal attenuation when comparing the Kärger model with the FPK model to be described next.

The Kärger ODEs with constant coefficients are easy to solve analytically or numerically. For the two-compartment case ($P = 2$, i.e. one extracellular compartment Ω^1 and one intracellular compartment Ω^2), the Kärger dMRI signal is given explicitly,

$$S_{\mathrm{KAR}}(b) = \rho\exp(-D_+q^2t)+(1-\rho)\exp(-D_-q^2t),$$

where

$$\begin{aligned} q &\equiv \delta\gamma\|\mathbf{g}\|, \\ D_\pm &\equiv \frac{1}{2}\Bigg((D^1_{\mathbf{g}}+D^2_{\mathbf{g}})+\frac{1}{q^2}\left(\frac{1}{\tau_{12}}+\frac{1}{\tau_{21}}\right) \\ &\quad \pm\sqrt{\left((D^2_{\mathbf{g}}-D^1_{\mathbf{g}})+\frac{1}{q^2}\left(\frac{1}{\tau_{21}}-\frac{1}{\tau_{12}}\right)\right)^2+\frac{4}{q^4\tau_{12}\tau_{21}}}\Bigg), \\ \rho &\equiv \frac{(v^1D^1_{\mathbf{g}}+v^2D^2_{\mathbf{g}})-D_-}{D_+-D_-}. \\ D^m_{\mathbf{g}} &= \mathbf{g}^T\overline{D}^m\mathbf{g}/\|\mathbf{g}\|^2 \end{aligned}$$

2.3. Macroscopic FPK model

In Coatléven *et al* (2014), a macroscopic FPK model was obtained from the microscopic multiple-compartment Bloch–Torrey PDE (1)–(6) using the periodic homogenization theory. The narrow pulse assumption on the diffusion encoding sequence was not needed. The Kärger model can be retrieved from the FPK model in the narrow pulse limit: $\delta \ll \Delta$.

The FPK model describes the time evolution of the compartment magnetizations as

$$\begin{aligned} \frac{\mathrm{d}\overline{M}^m_{\mathrm{FPK}}(b,t)}{\mathrm{d}t} = &-\left(c(t)\gamma^2\mathbf{g}^T\overline{D}^m\mathbf{g}+\sum_{l=1,\,l\neq m}^{P}\frac{1}{\tau^{lm}}\right)\overline{M}^m_{\mathrm{FPK}}(b,t) \\ &+\sum_{l=1,\,l\neq m}^{P}\frac{1}{\tau^{ml}}\overline{M}^l_{\mathrm{FPK}}(b,t), \quad m=1,\cdots,P, \end{aligned} \tag{15}$$

where the function $c(t)$ was derived in Coatléven *et al* (2014) to be

$$c(t):=\left(\int_0^t f(s)\mathrm{d}s\right)^2 \tag{16}$$

for any profile $f(t)$. For the standard PGSE sequence from equation (10), one finds

$$c(t)=\begin{cases}(t-t_s)^2, & t_s\le t\le t_s+\delta,\\ \delta^2, & t_s+\delta<t\le t_s+\Delta,\\ (t-\Delta-\delta-t_s)^2, & t_s+\Delta<t\le t_s+\Delta+\delta.\end{cases} \tag{17}$$

In the narrow pulse regime, $\delta \ll \Delta$, equation (17) yields the coefficient δ^2 of the Kärger model.

For connected $\Omega^l \in C$, the derivation of (Coatléven *et al* 2014) shows that

$$\frac{1}{\tau^{ml}}:=\kappa\frac{|\Gamma^{ml}|}{|\Omega^l|}, \quad (l\neq m), \tag{18}$$

from which

$$\frac{\tau^{lm}}{\tau^{ml}} = \frac{|\Omega^m|}{|\Omega^l|} = \frac{v^m}{v^l}, \tag{19}$$

where $|I^{ml}|$ is the surface area of the interface between Ω^m and Ω^l.

The initial condition of the FPK model is the same as for the Kärger model, namely, equation (14) and the dMRI signal is

$$S_{\mathrm{FPK}}(b) = \sum_{l=1}^{P} \overline{M}^{l}_{\mathrm{FPK}}(b, \mathrm{TE}). \tag{20}$$

2.4. Effective diffusion tensors

Now we define the effective diffusion tensors describing diffusion in the compartments in the long time limit. When the computational box C is small compared to the diffusion distance and under the assumption that C is periodically repeated, the effective diffusion tensor $\overline{D}^m$ in compartment Ω^m can be rigorously defined as (Coatléven *et al* 2014)

$$\overline{D}^m_{j,k} = \frac{1}{v^m} \int_{\Omega^m} D^0 \nabla W_j(\mathbf{r}) \cdot \mathbf{e}_k \, \mathrm{d}\mathbf{r}, \quad j,k = 1, \cdots, 3, \tag{21}$$

where $\mathbf{e}_k$ is the unit vector in the kth direction; one has to solve three Laplace equations over C for three unknown functions W_j:

$$\nabla \cdot \left(D^0 \nabla W_j(\mathbf{r}) \right) = 0, \quad \mathbf{r} \in \Omega^m, \quad j = 1, \cdots, 3, \tag{22}$$

subject to *impermeable* interface condition on $\partial\Omega^m$:

$$\nabla W_j(\mathbf{r}) \cdot \mathbf{n}(\mathbf{r}) = 0, \quad \mathbf{r} \in \partial\Omega^m, \tag{23}$$

and the following boundary conditions on ∂C:

$$W_j(\mathbf{r})\big|_{r_k = -L_k/2} = W_j(\mathbf{r})\big|_{r_k = L_k/2} - \delta_{j,k} L_k, \; k = 1, \cdots, 3, \tag{24}$$

$$\frac{\partial}{\partial r_k} W_j(\mathbf{r})\Big|_{r_k = -L_k/2} = \frac{\partial}{\partial r_k} W_j(\mathbf{r})\Big|_{r_k = L_k/2}, \quad k = 1, \cdots, 3, \tag{25}$$

where $\delta_{j,k} = 1$ if $k = j$ and $\delta_{j,k} = 0$, otherwise.

It is easy to show that if Ω^m is the union of spheres then its effective diffusion tensor vanishes:

$$\overline{D}^m = 0. \tag{26}$$

In other words, restricted diffusion in a compact *isolated* region becomes negligible in the long time limit.

We note that the expressions (18) and (26) have been used in previous works for the Kärger model (for example, in Fieremans *et al* (2010)).

2.5. Limiting cases

If there is no exchange between the compartments, the macroscopic dMRI signal under the Gaussian phase approximation is

$$S_{\mathrm{NOEX}}(b) = \sum_{m=1}^{P} v^m \exp(-D_{\mathbf{g}}^m b) \ , \tag{27}$$

where the effective diffusivity in compartment m in the gradient direction $\mathbf{u_g} \equiv \mathbf{g}/|\mathbf{g}|$ is

$$D_{\mathbf{g}}^m \equiv \mathbf{u_g}^T \overline{D}^m \mathbf{u_g}.$$

In the opposite limit of complete exchange, the macroscopic dMRI signal is

$$S_{\mathrm{COMPEX}}(b) = \exp\left(-\left(\sum_{m=1}^{P} v^m D_{\mathbf{g}}^m\right) b\right). \tag{28}$$

The Kärger model and the FPK model are formulated to investigate the intermediate exchange regime that falls between the two extreme cases in equations (27) and (28).

One important property of the FPK model (and its narrow pulse limit, the Kärger model) is that the apparent diffusion coefficient (ADC) extrapolated at $b = 0$, i.e.

$$\mathrm{ADC}_0 = \lim_{b \to 0} \frac{-\log S(b)}{b},$$

is independent of time and of the permeability κ:

$$\mathrm{ADC}_0^{\mathrm{KAR}} = \mathrm{ADC}_0^{\mathrm{FPK}} = \mathrm{ADC}_0^{\mathrm{COMPEX}} = \mathrm{ADC}_0^{\mathrm{NOEX}} = \sum_{m=1}^{P} v^m D_{\mathbf{g}}^m \, .$$

Thus, two necessary conditions for the applicability of the above macroscopic models are: (i) the diffusion time should be long enough that the measured ADC_0 does not change (much) with time and (ii) the cell membrane permeability κ should be low enough that it does not affect (much) the ADC_0.

2.6. Quality of macroscopic models

We constructed the computational box $C = [-5\ \mu\mathrm{m},\ 5\ \mu\mathrm{m}]^3$ shown in figure 1 containing 76 spherical cells with a range of radii between 0.6 μm and 2.55 μm. Formally, one could consider 76 different compartments for the 76 spheres, each with its volume fraction and surface-to-volume ratio. However, we just combine the 76 spheres to form one compartment Ω^2. The remaining extracellular space forms another compartment Ω^1. The corresponding volume fractions are $v^2 = 0.65$ and $v^1 = 0.35$. The surface-to-volume ratio is $|\Gamma^{21}|/|\Omega^2| = 1.85\ \mu\mathrm{m}^{-1}$. We consider that $|\Gamma^{21}|/|\Omega^2|$ is a good approximation of the average surface-to-volume ratios of all the 76 spheres. Note that this approximation would be exact if all the spheres had the same radius.

Setting the intrinsic diffusion coefficient $D^0 = 3 \times 10^{-3}\ \mathrm{mm}^2\ \mathrm{s}^{-1}$ and the permeability $\kappa = 10^{-5}\ \mathrm{m\ s}^{-1}$, one finds the true model parameters to be

$$\mathcal{U}_{\mathrm{true}} = \left\{ v^2 = 0.65, D_{\mathbf{g}}^1 = 2.20 \times 10^{-3}\,\mathrm{mm}^2\,\mathrm{s}^{-1}, \overline{D}^2 = 0, \tau^{12} = 54\,\mathrm{ms} \right\}, \tag{29}$$

where the true value of $D_{\mathbf{g}}{}^1$ is computed numerically as earlier explained in section 2.4. The value $D_{\mathbf{g}}{}^1 = 2.20 \times 10^{-3}\ \mathrm{mm}^2\ \mathrm{s}^{-1}$ is rather high compared to the values found in the literature for brain tissue due to the geometry chosen (spherical cells).

We first check the quality of the macroscopic models as an approximation of the 'ground truth' dMRI signal obtained from the Bloch–Torrey equation. Figure 1(*b*) shows that the

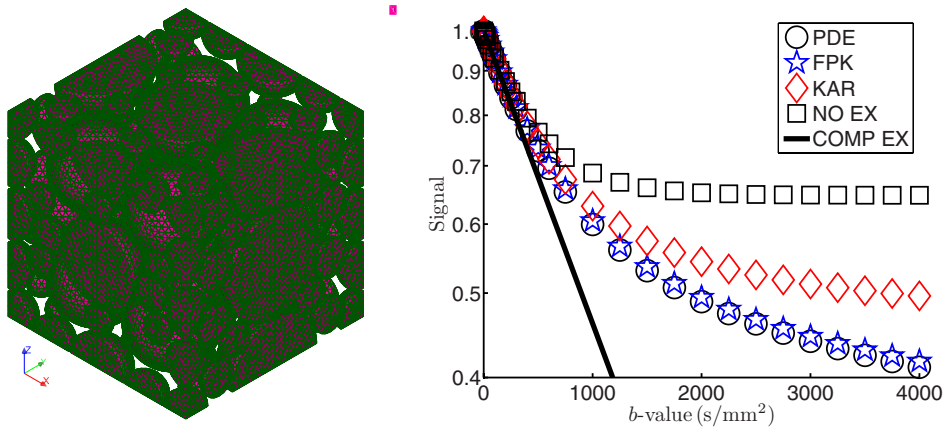

Figure 1. (*a*) The computational box $C = [-5\ \mu\text{m}, 5\ \mu\text{m}]^3$ contains 76 spheres with radii between 0.6 μm and 2.55 μm. The volume fraction of the spheres and of the extracellular space are $v^2 = 0.65$ and $v^1 = 0.35$, respectively. We set $\kappa = 10^{-5}$ m s^{-1}, $D^0 = 3 \times 10^{-3}$ mm^2 s^{-1}. (*b*) The dMRI signals: $S_{\text{PDE}}(b)$, $S_{\text{FPK}}(b)$, $S_{\text{KAR}}(b)$, $S_{\text{NOEX}}(b)$, $S_{\text{COMPEX}}(b)$. The parameters of the PGSE sequence are $\delta = \Delta = 40$ ms.

two-compartment FPK model gives a good approximation of the signal from the Bloch–Torrey PDE. For the PGSE sequence with $\delta = \Delta = 40$ ms, the narrow pulse assumption is not satisfied and the original Kärger model fails to approximate the dMRI signal. In turn, the FPK model provides a very accurate approximation over the typical range of b-values up to 4000 s mm^{-2}.

3. Materials and methods

The parameter estimation consists of fitting an experimentally measured dMRI signal to an appropriate macroscopic model in order to extract the model parameters. In order to investigate the sensitivity and robustness of the parameters estimation problem, we replace experimental data by synthetically generated data to which we added Gaussian noise in the real and imaginary parts. This allows us to check the influence of various factors on the stability and the quality of the parameters estimation.

We show results for two examples. In the first example, the synthetic dMRI data is generated by solving the FPK model for the 76-spheres geometry using the true model parameters in equation (29) (see section 2.6). In the second example, the synthetic dMRI data is obtained by evaluating the bi-exponetial fit of published *in vivo* data in the rat brain cortex (Pyatigorskaya *et al* 2014).

3.1. Synthetic dMRI signal

3.1.1. First example. For the 76-spheres example (see section 2.6) we generated the dMRI signal by using the FPK model with the true parameters in equation (29) and simulating two PGSE sequences with

$$\{\delta = \Delta = 25\,\text{ms};\ \delta = \Delta = 40\,\text{ms}\}\,. \tag{30}$$

3.1.2. Second example. For our second example, we refer to the *in vivo* experimental signals of the rat cortex obtained for PGSE at $\delta = 2.5$ ms and several diffusion times (Pyatigorskaya *et al* 2014). Here we focus on two diffusion times: $\Delta = 10$, 30 ms. It was shown that the experimental data over b-values in the range [0, 4000] s mm^{-2} can be well fitted using a bi-exponential function:

$$S = f^s \exp(-bD^s) + (1 - f^s)\exp(-bD^f),$$

where the values are as shown below.

δ, ms	Δ, ms	f^s	D^f, mm^2 s^{-1}	D^s, mm^2 s^{-1}
2.5	10	0.27	0.89×10^{-3}	0.23×10^{-3}
2.5	30	0.32	0.92×10^{-3}	0.29×10^{-3}

We use the above bi-exponential description to generate dMRI signals and we simulate the same PGSE sequences as in the *in vivo* experiment:

$$\{\delta = 2.5\,\text{ms}, \Delta = 10\,\text{ms};\ \delta = 2.5\,\text{ms}, \Delta = 30\,\text{ms}\}\,. \tag{31}$$

For both examples, the dMRI signals were computed at a set of 42 b-values:

$$b_k = \begin{cases} 50k\ \text{s mm}^{-2}, & k = 1 \ldots 5, \\ 100(k-3)\ \text{s mm}^{-2}, & k = 6 \ldots 42\,. \end{cases} \tag{32}$$

Note the first few low b-values increase in intervals of 50 s mm^{-2} (e.g. $b_1 = 50$ s mm^{-2}, $b_2 = 100$ s mm^{-2}, etc) and the later b-values increase in intervals of 100 s mm^{-2} (e.g. $b_6 = 300$ s mm^{-2}, $b_7 = 400$ s mm^{-2}, etc). The set of b-values is within the range typically used in experimental settings for brain imaging. We denote by $S(b_k)$ the simulated dMRI signal at b_k.

3.2. Noisy signal

In order to quantify the effect of experimental noise in the parameters estimation problem, we add Gaussian noise to the real and imaginary components of the simulated signal $S(b_k)$ to produce noisy signals:

$$S_{\sigma,i}(b_k) = \sqrt{\left(S(b_k) + \sigma\mathcal{N}_{i,k}^{\text{Re}}\right)^2 + \left(\sigma\mathcal{N}_{i,k}^{\text{Im}}\right)^2}\,, \tag{33}$$

where $k = 1, \cdots, 42$ (42 b-values), $i = 1, \cdots, N$ (N random samples of noisy signal), σ is the level of noise, while $\mathcal{N}_{i,k}^{\text{Re}}$ and $\mathcal{N}_{i,k}^{\text{Im}}$ are independent Gaussian variables with zero mean and unit variance. In practice, we save all generated noises $\mathcal{N}_{i,k}^{\text{Re}}$ and $\mathcal{N}_{i,k}^{\text{Im}}$ for $N = 1000$ samples of noise and use them repeatly when comparing different noise levels and parameters estimation strategies. We will generate results for 5 different noise levels

$$\sigma \in \{0.0125, 0.025, 0.05, 0.1, 0.2\}.$$

Note that the imaginary part of the simulated signal $S(b_k)$ is zero due to the rephasing of the nuclei.

The above scheme of adding Gaussian noises to the real and imaginary parts of the signal results in the so-called Rice distributed noisy magnitude signal (see, for example, Gudbjartsson and Patz (1995)) which is considered a benchmark for dMRI measurements. In other words,

the noisy magnitude signal $S_{\sigma,i}(b_k)$ from equation (33) is a random variable from the Rice distribution (Rice 1944). The expected value and the variance of this variable are

$$\langle S_{\sigma,i}(b_k)\rangle = \sigma F(S(b_k)/\sigma), \tag{34}$$

$$\mathrm{var}\{S_{\sigma,i}(b_k)\} = \sigma^2(2+[S(b_k)/\sigma]^2-[F(S(b_k)/\sigma)]^2), \tag{35}$$

where

$$F(x)=\sqrt{\pi/2}\ \mathrm{e}^{-x^2/4}[(1+x^2/2)I_0(x^2/4)+(x^2/2)I_1(x^2/4)], \tag{36}$$

and $I_n(z)$ are the modified Bessel functions of the first kind. When $\sigma \ll S(b_k)$ (i.e. $x \gg 1$), one gets

$$F(x)\simeq x+\frac{1}{2x}+\frac{1}{8x^3}+O(x^{-5}) \tag{37}$$

so that the mean value $\langle S_{\sigma,i}(b_k)\rangle$ approaches the noiseless signal $S(b_k)$ as expected. One can check that this approximate relation is accurate within 5% even at $x = 1$ (i.e. when $S(b) = \sigma$), while its relative error is 0.3% at $x = 2$.

In the opposite limit $\sigma \gg S(b_k)$ (i.e. $x \ll 1$), $F(x)\simeq \sqrt{\pi/2}\,(1+O(x^2))$ so that $\langle S_{\sigma,i}(b_k)\rangle \to \sqrt{\pi/2}\ \sigma$. In other words, when the noise level is too large as compared to the noiseless signal, one measures the noise level. This situation is not relevant in practice.

According to equation (35), the variance of the noisy signal monotonously grows from $\sigma^2(2-\pi/2)\approx 0.43\sigma^2$ at $x = 0$ to σ^2 at $x = \infty$. One can conclude that the variance does not change significantly, even for very noisy signals.

It is also convenient to define the signal-to-noise ratio as

$$\mathrm{SNR}_k=\frac{\langle S_{\sigma,i}(b_k)\rangle}{\sqrt{\mathrm{var}\left\{S_{\sigma,i}(b_k)\right\}}}=\frac{S(b_k)}{\sigma}\,\tilde{F}(S(b_k)/\sigma), \tag{38}$$

where

$$\tilde{F}(x)=\frac{1}{x}\left(\frac{2+x^2}{[F(x)]^2}-1\right)^{-1/2}. \tag{39}$$

Using equation (37) for large x, the correction factor $\tilde{F}(x)$ can be written as

$$\tilde{F}(x)\simeq 1+\frac{3}{4x^2}+\frac{13}{32x^4}+O(x^{-6}). \tag{40}$$

For instance, $\tilde{F}(5)\simeq 1.03$. In other words, when x is large, SNR_k is close to $S(b_k)/\sigma$, as expected.

For the first example (76-spheres), figure 2(*a*) shows the bias of the signal at $\sigma = 0.2$. One can see that the presence of noise tends to increase the signal: mean values of noisy signal (shown by circles and by solid line) lie above the noiseless signal (shown by dashed line). While this bias is negligible for small σ (not shown), it cannot be ignored at noises as large as $\sigma = 0.2$. Figure 2(*b*) presents the signal-to-noise ratio from equation (38) for all σ and $\delta = \Delta = 40$ ms.

The decrease of the dMRI signal $S(b)$ with b-values results in decreasing SNR at large b-value. At the highest considered noise level $\sigma = 0.2$, SNR remains around 5 for almost all b-values.

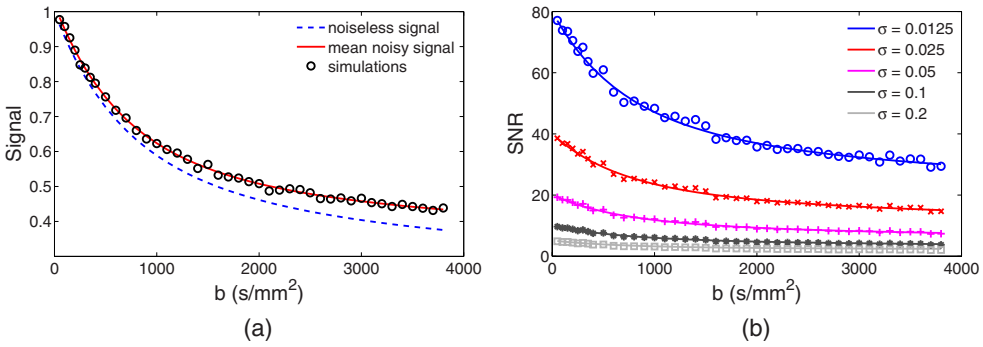

Figure 2. First example (76-spheres geometry) with $\delta = \Delta = 40$ ms: (*a*) Comparison between $S(b)$ (noiseless signal) and $\langle S_{\sigma,i}(b)\rangle$ (mean noisy signal); (*b*) SNR. Signal $S(b)$ is obtained by solving the FPK model using the true model parameters for the 76-spheres geometry. Symbols show the empirical mean values of $S_{\sigma,i}(b)$ over 1000 realizations.

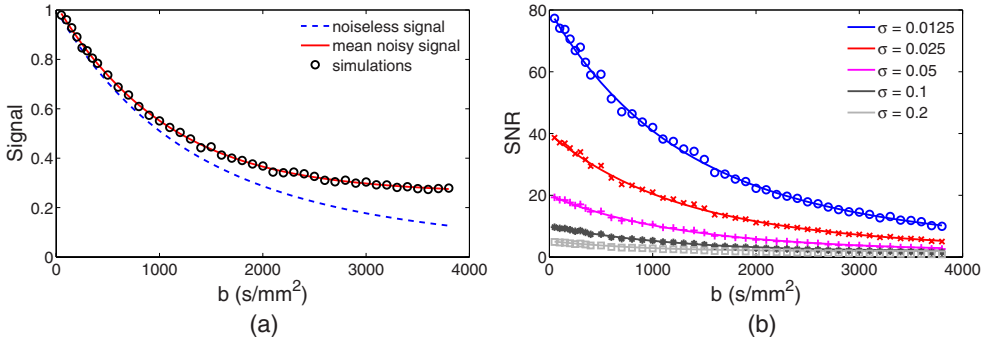

Figure 3. Second example (adapted from *in vivo* data) for $\delta = 2.5$ ms, $\Delta = 10$ ms: (*a*) Comparison between $S(b)$ (noiseless signal) and $\langle S_{\sigma,i}(b)\rangle$ (mean noisy signal); (*b*) SNR. Signal $S(b)$ is obtained using bi-exponential fit from *in vivo* rat brain cortex experimental data. Symbols show the empirical mean values of $S_{\sigma,i}(b)$ over 1000 realizations.

For the second example (bi-exponential fit of rat cortex data), figure 3(*a*) shows the bias of the signal at $\sigma = 0.2$, $\delta = 2.5$ ms, $\Delta = 10$ ms. As earlier, the presence of noise tends to increase the signal. Figure 3(*b*) presents the signal-to-noise ratio (SNR) as a function of b-value for all σ, at $\delta = 2.5$ ms, $\Delta = 10$ ms.

To perform the parameters estimation on noisy data using a subset, $\mathcal{K} \subset \{1, \cdots, 42\}$, of b-values, we define the SNR as SNR_1, i.e. the signal-to-noise ratio at the smallest (nonzero) b-value that we use: $b_1 = 50$ s mm^{-2}.

3.3. The least squares problem

In order to estimate the FPK model parameters, we fit the noisy signal to the FPK model in a weighted least squares (WLS) sense.

For the first example, the 4-parameter set to be estimated is

$$\mathcal{U} = \left\{s_0, v^2, D_{\mathrm{g}}^1, \tau^{12}\right\}, \tag{41}$$

where the residence time τ^{12} is related to the permeability κ according to equation (18) and $D_{\mathbf{g}}{}^1$ is the extracellular effective diffusion coefficient in direction $\mathbf{g} = (1, 0, 0)$, s_0 is the extrapolated value of the dMRI signal at $b = 0$. The other parameters of the FPK model are retrieved as

$$\begin{aligned}
&\frac{\tau^{12}}{\tau^{21}} = \frac{v^2}{v^1},\\
&v^1 + v^2 = 1,\\
&\overline{D}^2 = 0, \text{because } \Omega^2 \text{ is the union of spheres.}
\end{aligned}$$

For the second example, we note that the effective diffusion coefficients of two compartments have to be found. This is different from the spheres example where $\overline{D}^2$ was set to zero. To shorten the computational time, we set s_0 to its true value ($s_0 = 1$) and the 4-parameters set to be estimated for this example is

$$\mathcal{U} = \left\{v^2, D^1_{\mathbf{g}}, D^2_{\mathbf{g}}, \tau^{12}\right\}. \tag{42}$$

For a given set $\mathcal{U}$ of macroscopic model parameters, we denote the FPK signal by $S_{\text{FPK}}(b, \mathcal{U})$. For each random sample of noisy signal $S_{\sigma,i}(b)$, we solve the following least squares problem:

$$\min_{\mathcal{U}} \sum_{k\in\mathcal{K}} \left|S_{\sigma,i}(b_k) - s_0 S_{\text{FPK}}(b_k, \mathcal{U})\right|^2 w_k, \tag{43}$$

where $\mathcal{K} \subset \{1, \cdots, 42\}$ is a subset of the full list of simulated b-values and w_k are the associated weights. The solution of equation (43) which is denoted as $\mathcal{U}^i_{\text{FPK}}$, is random because it depends on a random realization of a noisy signal. Repeating this procedure for $N = 1000$ samples, we compute the mean values (MV) of the estimated parameters and their standard deviations (SD). In what follows, we focus on two cases: identical weights $w_k = 1$ and $w_k = 1/\text{var}\{S_{\sigma,i}(b_k)\}$ from equation (35).

3.4. Numerical resolution

In order to assess the quality and robustness of the parameters estimation with the FPK model, we perform the following analysis.

(a) We solve the least squares problem in equation (43) by an exhaustive search in the parameter space.

- For the first example, the 4D parameter space is $\mathcal{U} = \{s_0, v^2, D^1_{\mathbf{g}}, \tau^{12}\}$. The limits of the search space were chosen to be

$$[0.9, 1.1] \times U_3,$$

where the limits U_3 for $\{v^2, D^1_{\mathbf{g}}, \tau^{12}\}$ are

$$U_3 = \{[0.4,\ 0.9]\} \times \{[1.0,\ 3.0] \times 10^{-3}\,\text{mm}^2\,\text{s}^{-1}\} \times \{[1,\ 150]\,\text{ms}\}.$$

We created and saved a search table for U_3 that has the values of $S_{\text{FPK}}(b_k, \mathcal{U})$, $k = 1, \cdots, 42$, with a uniform discretization in 51 points in [0.4, 0.9], 41 in $[1.0, 3.0] \times 10^{-3}$ mm^2 s^{-1} and 150 in [1, 150] ms. Previously, the idea of using search tables for parameter estimation in dMRI has appeared in Iima *et al* (2015). The exhaustive search for s_0 was conducted in [0.9, 1.1] using 9 uniform discretization points. The range for s_0 is justified because the synthetic signal is already normalized to $S(b = 0) = 1$. In summary, the precision of our search method is 0.05×10^{-3} mm^2 s^{-1} in $D_{\mathbf{g}}{}^1$, 0.01 in v^2, 1 ms in τ^{12} and 0.025 in s_0.

The ODE system (21) in the FPK model is solved numerically in Matlab by the function ode45 with absolute and relative tolerances of 10^{-6}.

- For the second example, we conduct an exhaustive search in 4D parameter space for $\mathcal{U} = (v^2, D_{\mathbf{g}}^1, D_{\mathbf{g}}^2, \tau^{12})$. The limits of the search space were chosen to be:

$$\begin{aligned} U_4 &= \{[0.25,\ 0.55]\} \times \{[0.5,\ 3.0] \times 10^{-3}\,\mathrm{mm^2\,s^{-1}}\} \\ &\times \{[0,\ 0.5] \times 10^{-3}\,\mathrm{mm^2\,s^{-1}}\} \times \{[1,\ 400]\,\mathrm{ms}\}, \end{aligned}$$

We created and saved a search table for U_4 that had the values of $S_{\mathrm{FPK}}(b_k, \mathcal{U})$, $k = 1, \cdots, 42$, with a uniform discretization in 31 points in [0.25, 0.55], 51 in [0.5, 3.0] $\times 10^{-3}$ mm^2 s^{-1} for $D_{\mathbf{g}}^1$, 11 in [0.0, 0.5] $\times 10^{-3}$ mm^2 s^{-1} for $D_{\mathbf{g}}^2$, and 400 in [1, 400] ms. The precision of the search table is the same as for the first example. Because δ is much smaller than Δ, it is sufficient to use the Kärger model for the second example.

(b) We characterize the quality of the fit by the root of the mean squared error (RMSE) of the weighted LS fitting, normalized by the weights,

$$\mathrm{RMSE}_i = \sqrt{\frac{\sum_{k\in\mathcal{K}} \left| S_{\sigma,i}(b_k) - s_0 S_{\mathrm{FPK}}(b_k, \mathcal{U}) \right|^2 w_k}{\sum_{k\in\mathcal{K}} w_k}}\,. \tag{44}$$

This quantity characterizes the accuracy of the LS fitting for one random realization of the noisy signal. In what follows, we will present the empirical mean values and the standard deviations of the estimated parameters and of RMSE_i after averaging over 1000 realizations, as functions of the noise level (plotted against the SNR from equation (38)). In addition, for the first example, because the true values of the FPK model parameters are known, the mean values of the estimated parameters are compared to their true values. Note that while the true values of v^2 and τ^{12} are determined by the microstructure and the permeability, the true value of $D_{\mathbf{g}}{}^1$ is computed from equation (21) by solving numerically equations (22)–(24) by the same finite elements method as for the Bloch–Torrey equation (Nguyen *et al* 2014).

4. Results and discussion

4.1. First example

We compare four parameters estimation strategies:

- Choice 1: sequence $\delta = \Delta = 40$ ms, the full list of 42 b-values in equation (32), LS weighting $w_k = 1$;
- Choice 2: sequence $\delta = \Delta = 40$ ms, the full list of 42 b-values in equation (32), LS weighting $w_k = 1/\mathrm{var}\{S_{\sigma,i}(b_k)\}$ from equation (35);
- Choice 3: Sequence $\delta = \Delta = 25$ ms, the full list of 42 b-values in equation (32), LS weighting $w_k = 1$;
- Choice 4: sequence $\delta = \Delta = 40$ ms, b-values are taken from the first 21 of the 42 values in equation (32) and repeated once (for a total of 42 b-values, 21 of them distinct), LS weighting $w_k = 1$. The b-values range from 50 s mm^{-2} to 1700 s mm^{-2}.

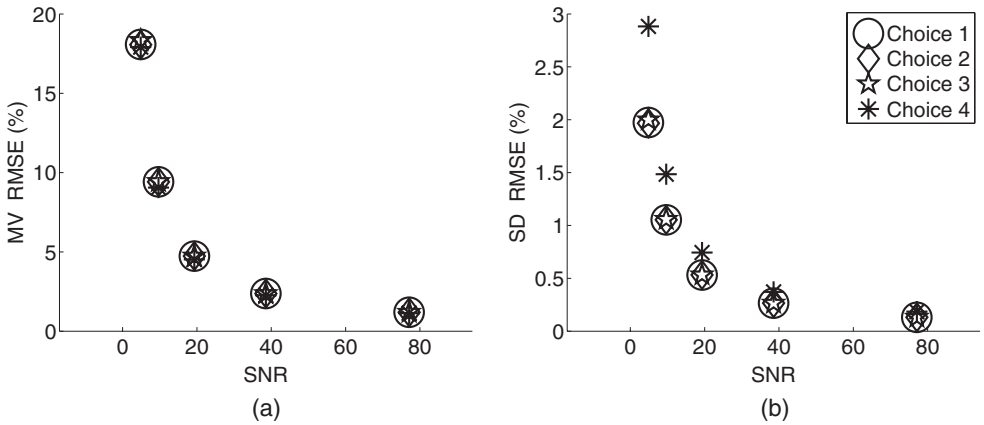

Figure 4. Comparison between four strategies described in section 4.1 for the 76-spheres example: empirical mean values (MV, as a percentage) in (*a*) and standard deviations (SD, as a percentage) in (*b*) of RMSE as functions of the SNR at the lowest *b*-value. The SNR is defined in equation (38).

In this way, we compare the reference case (Choice 1) with other cases in order to reveal the respective roles of weighting by the reciprocal of the variance (Choice 2), using shorter diffusion time (Choice 3) and using a smaller range of *b*-values (Choice 4).

First we show in figure 4 the normalized RMSE defined in equation (44). One can see that all four strategies provide similar RMSE, both in the mean values and the standard deviations. The mean values of the RMSE increased from 1% at SNR = 100 to 18% at SNR = 4.9. The standard deviations increase from 0.1% to 3%.

In figure 5 we show the mean values and standard deviations (as percentages) of the parameters, $D_{\mathbf{g}}{}^1$, v^2, τ^{12}, of the four strategies (the parameters are normalized by their true values for convenience). We see that

(a) As the SNR decreases from 77 to 4.9, for Choices 1 and 2, the mean values of $D_{\mathbf{g}}{}^1$ decrease from 101% to 96% of the true values. For Choice 3, the mean values decrease from 102% to 98% of the true value. For Choice 4, the mean value decreases from 102% to 93% of the true values. For Choices 1 and 2, the standard deviations of $D_{\mathbf{g}}{}^1$ increase from 23% to 26% of the true values. For Choice 3, the standard deviations increase from 20% to 35% of the true values. For Choice 4, the standard deviations increase from 30% to 40% of the true values.

(b) As the SNR decreases from 77 to 9.7, for Choices 1 and 2, the mean values of v^2 decrease from 98% to 92% of the true values. For Choice 3, the mean values decrease from 100% to 95% of the true values. For Choice 4, the mean values decrease from 96% to 93% of the true values. For Choices 1 and 2, the standard deviations of v^2 increase from 10% to 21% of the true values. For Choice 3, the standard deviations increase from 8% to 19% of the true values. For Choice 4, the standard deviations increase from 15% to 18% of the true values.

(c) As the SNR decreases from 77 to 4.9, for Choices 1, 2 and 3, the mean values of τ^{12} increase from 110% to 185% of the true values. For Choice 4, the mean values increase from 140% to 155% of the true values. For Choices 1, 2 and 3, the standard deviations of τ^{12} increase from 30% to 100% of the true values. For Choice 4, the mean values increase from 70% to 120% of the true values.

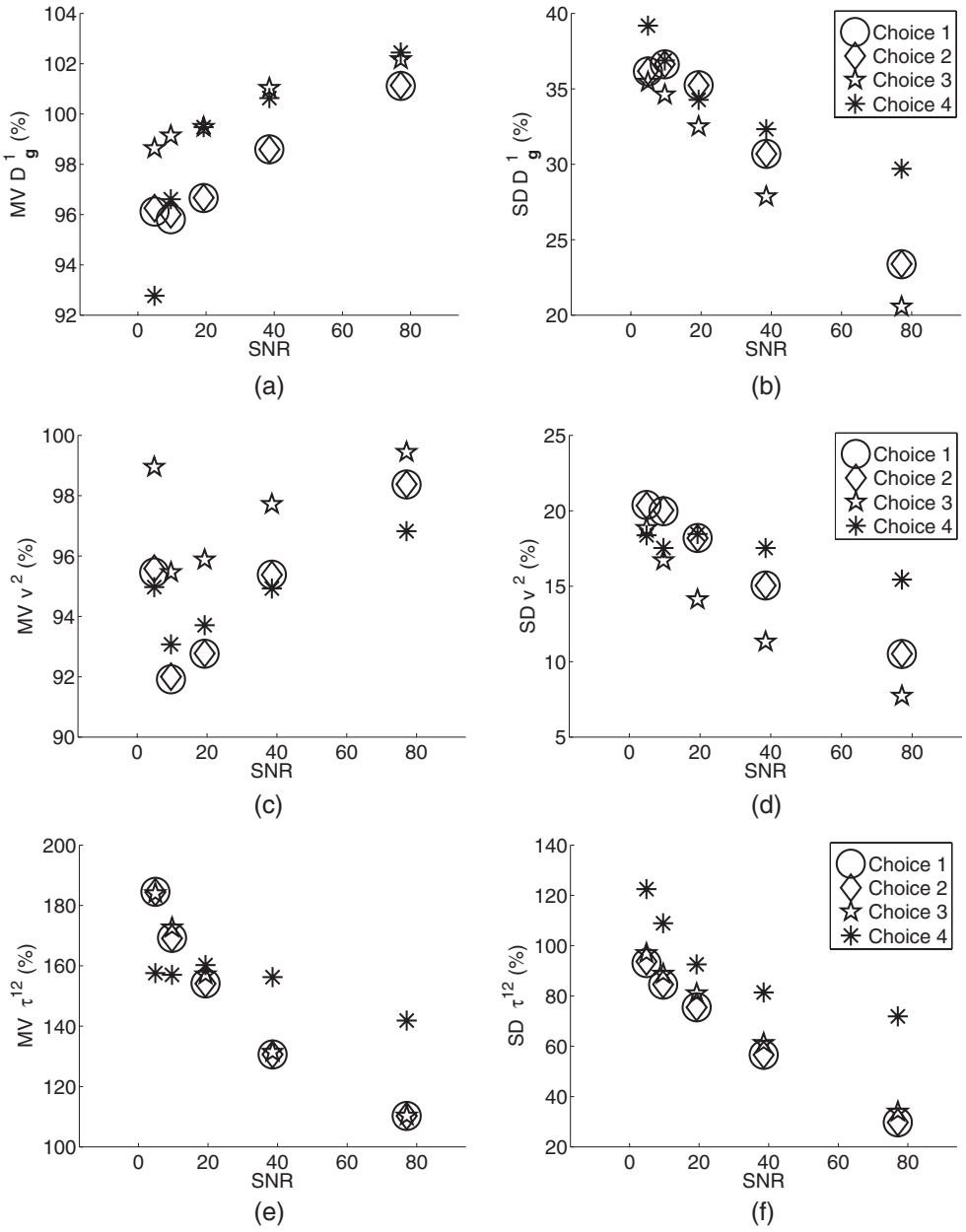

Figure 5. Comparison between four strategies described in section 4.1 to estimate $\{s_0, D_{\mathbf{g}}{}^1, v^2, \tau^{12}\}$ for the 76-spheres example. Results from 1000 samples of noisy signals for 5 noise levels. The empirical mean values and standard deviations of the estimated parameters: $D_{\mathbf{g}}{}^1$, v^2, τ^{12}, normalized by their true values from equation (29), are shown as functions of the SNR (at the lowest b-value). The SNR is defined in equation (38). (*a*) MV $\frac{D_{\mathbf{g}}^1}{(D_{\mathbf{g}}^1)_{\text{true}}}$. (*b*) SD $\frac{D_{\mathbf{g}}^1}{(D_{\mathbf{g}}^1)_{\text{true}}}$. (*c*) MV $\frac{v^2}{v^2_{\text{true}}}$. (*d*) SD $\frac{v^2}{v^2_{\text{true}}}$. (*e*) MV $\frac{\tau^{12}}{\tau^{12}_{\text{true}}}$. (*f*) SD $\frac{\tau^{12}}{\tau^{12}_{\text{true}}}$.

4.2. In vivo brain imaging

In figure 6 we compare the following four estimation strategies:

- Choice 1: sequence $\delta = 2.5$ ms, $\Delta = 30$ ms, the full list of 42 b-values in equation (32), LS weighting $w_k = 1$;
- Choice 2: sequence $\delta = 2.5$ ms, $\Delta = 30$ ms, the full list of 42 b-values in equation (32), LS weighting $w_k = 1/\mathrm{var}_k\{S_{\sigma,i}(b_k)\}$ from equation (35);
- Choice 3: sequence $\delta = 2.5$ ms, $\Delta = 10$ ms, the full list of 42 b-values in equation (32), LS weighting $w_k = 1$.
- Choice 4: sequence $\delta = 2.5$ ms, $\Delta = 30$ ms, b-values are taken from the first 21 of the 42 values in equation (32) and repeated once (for a total of 42 b-values, 21 of them distinct), LS weighting $w_k = 1$. The b-values range from 50 s mm^{-2} to 1700 s mm^{-2}.

Results from 1000 samples of noisy signals for 5 noise levels are shown. In figure 6 we show the mean values and standard deviations of the estimated parameters, $D^1_{\mathbf{g}}$, v^2, τ^{12}, $D^2_{\mathbf{g}}$, of the strategies described above. The mean values of the estimated parameters are not normalized by their true values as in the previous example because the true values are not known. The standard deviations of the estimated parameters are normalized by their mean values and expressed as a percentage. We see that

(a) As the SNR decreases from 77 to 4.9, for Choices 1, 2, 3, 4, the mean values of $D^1_{\mathbf{g}}$, increase from 1.0×10^{-3} mm^2 s^{-1} to 1.2×10^{-3} mm^2 s^{-1}. For Choices 1, 2, 3, the standard deviations of $D^1_{\mathbf{g}}$, increase from 15% to 40% of the mean value. For Choice 4, the standard deviations increase from 15% to 55% of the mean values.

(b) For Choices 1 and 2, the mean values of v^2 vary between 0.36 to 0.38. For Choice 3, the mean values vary between 0.35 to 0.37. For Choice 4, the mean values vary between 0.38 to 0.41. The trend of the mean values is not monotonic with SNR. For Choices 1, 2, 3, the standard deviations of v^2 vary between 30% to 38% of the mean values. For Choice 4, the standard deviations vary between 26% to 34% of the mean values.

(c) As the SNR decreases from 77 to 4.9, for Choices 1, 2, the mean values of τ^{12} increase from 70 ms to 225 ms. For Choice 3, the mean values increase from 30 ms to 160 ms. For Choice 4, the mean value increases from 70 ms to 160 ms. Between SNR = 9.7 and SNR = 77, for Choices 1, 2 and 4, the standard deviations of τ^{12} are around 120% of the mean values. Between SNR = 9.7 and SNR = 77, for Choice 3, the standard deviations of τ^{12} are around 180% of the mean values. There is a decrease in the normalized standard deviations at SNR = 4.9 because the mean values are very large.

(d) As the SNR decreases from 77 to 4.9, for Choices 1, 2, 3, the mean value of $D^2_{\mathbf{g}}$ decreases from 0.2×10^{-3} mm^2 s^{-1} to 0.05×10^{-3} mm^2 s^{-1}. For Choice 4, the mean values of $D^2_{\mathbf{g}}$ are around 2.5×10^{-3} mm^2 s^{-1}. For Choices 1, 2, 3, the standard deviations of $D^2_{\mathbf{g}}$ increase from 60% to 145% of the mean values. For Choice 4, the standard deviations increase from 55% to 90% of the mean values.

4.3. Bias-corrected signal

When the noise level σ is significant, the mean values of the noisy signal lie above the noiseless signal, as illustrated in figures 2 and 3. As a consequence, fitting noisy signals $S_{\sigma,i}(b)$ by the (noiseless) model signal $S_{\mathrm{FPK}}(b)$ may yield a strong bias in estimated parameters. This bias can be corrected by replacing the model signal $S_{\mathrm{FPK}}(b)$ by the expected value $\langle S_{\sigma,i}(b)\rangle = \sigma F(S_{\mathrm{FPK}}(b)/\sigma)$ from equation (34). When the noise level σ is not known *a priori*, it can be

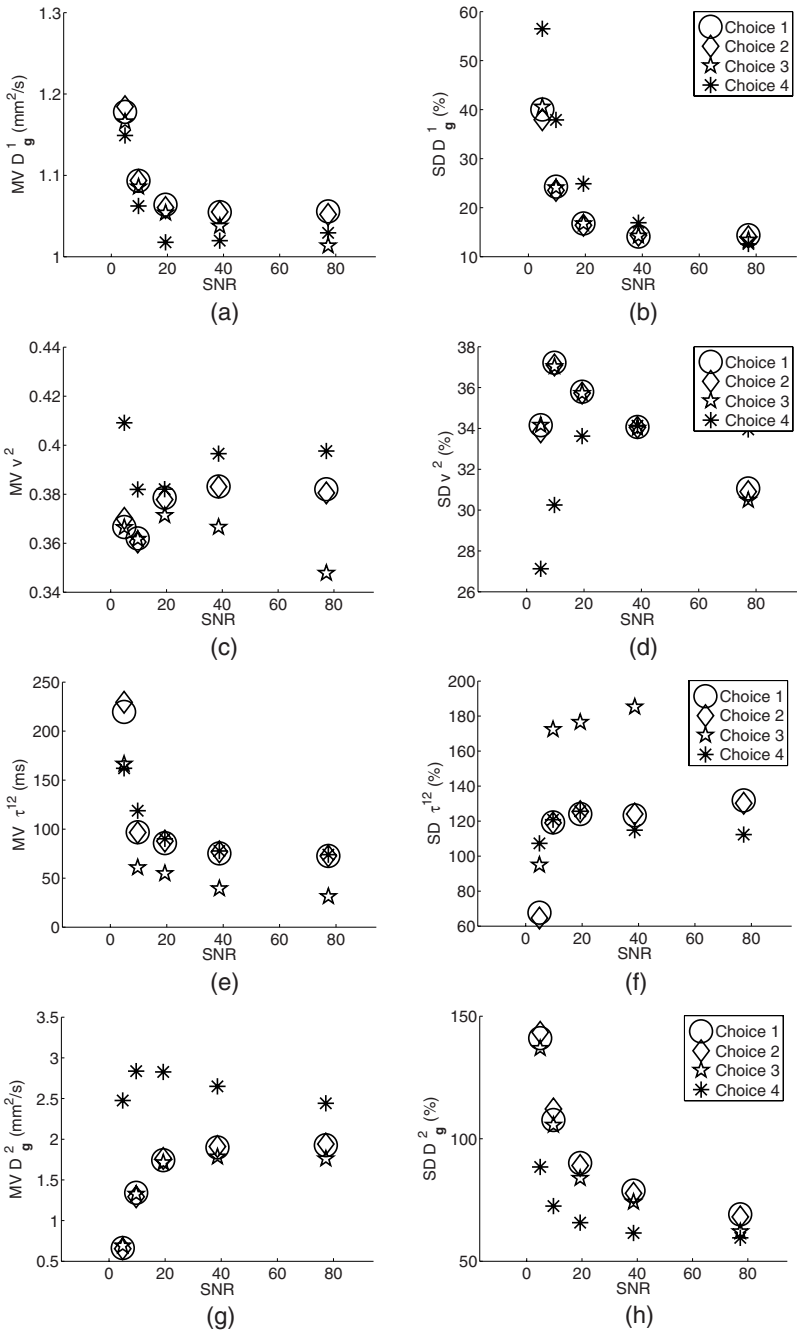

Figure 6. Comparison between four strategies described in section 4.2 to estimate $\{v^2, D_g{}^1, D_g{}^2, \tau^{12}\}$ for the *in vivo* rat brain cortex experimental data. Results from 1000 samples of noisy signals for 5 noise levels. The empirical mean values and standard deviations of the estimated parameters (v^2, $D_g{}^1$, $D_g{}^2$, τ^{12}), are shown as functions of the SNR at the lowest *b*-value. The SNR is defined in equation (38). The mean values are not normalized by the true values of the parameters as in the previous example since the true values are not known. The standard deviations of the estimated parameters are normalized by their mean values and expressed in percentages. (*a*) MV $D_g{}^1$ (mm^2 s^{-1}). (*b*) SD $D_g{}^1$ (%). (*c*) MV v^2. (*d*) SD v^2 (%). (*e*) MV τ^{12} (ms). (*f*) SD τ^{12} (%). (*g*) MV $D_g{}^2$ (mm^2 s^{-1}). (*h*) SD $D_g{}^2$ (%).

considered as an additional unknown parameter in the LS problem, i.e. added to macroscopic model parameters $\mathcal{U}$. We note that this simple correction method relies on the assumption of the Rician noise (from which equation (34) was derived). As discussed in Gudbjartsson and Patz (1995) and Veraart *et al* (2011), this assumption is satisfied in most dMRI measurements.

We compare three choices (for simplicity, s_0 will be set to 1 instead of being a searched parameter in the LS method also for the 76-spheres example, just like in the rat cortex example):

- 'No NC': no noise correction, in which case one solves the LS problem in equation (43) as in earlier sections;
- 'NC 1': noise correction with known noise level σ, in which case one solves the LS problem

$$\min_{\mathcal{U}} \sum_{k\in\mathcal{K}} \left|S_{\sigma,i}(b_k) - \sigma F(S_{\mathrm{FPK}}(b_k,\mathcal{U})/\sigma)\right|^2 w_k\,. \tag{45}$$

- 'NC 2': noise correction with unknown noise level σ, in which case the LS problem becomes

$$\min_{\mathcal{U},\beta} \sum_{k\in\mathcal{K}} \left|(S_{\sigma,i}(b_k) - \beta F(S_{\mathrm{FPK}}(b_k,\mathcal{U})/\beta)\right|^2 w_k, \tag{46}$$

  where β is an additional fitting parameter (the best fit noise level). The parameter β adds a new dimension to the search space. We used the following discretization of β in the global search:

$$\beta \in [0.5, 0.6, \cdots, 1.5]\times\sigma,$$

where σ is the true noise level.

In figure 7 we show the results for the 76-spheres example. We used the sequence $\delta = \Delta = 40$ ms, the full list of 42 b-values in equation (32), LS weighting $w_k = 1$. We see at SNR = 9.7, the small bias in $D_{\mathbf{g}}{}^1$ (96% of true value) is corrected by 'NC 1'(98% of true value) and 'NC 2'(98% of true value), with essentially no change in estimated v^2 and τ^{12}. At SNR = 4.9, the small bias in $D_{\mathbf{g}}{}^1$ (95% of true value) is corrected by 'NC 1'(98% of true value) and 'NC 2'(99% of true value), with an improvement in τ^{12}, going from 190% of the true value to 160% for 'NC 1' and 135% for 'NC 2' and a worse estimated v^2: going from 96% of the true value to 91% for 'NC 1' and 90% for 'NC 2'. There is very little change in the standard deviations.

In figure 8 we show the results for the rat cortex bi-exponential fit example. We used the sequence δ = 2.5 ms, Δ = 30 ms, the full list of 42 b-values in equation (32), LS weighting w_k = 1. We see at the smallest SNR shown (= 4.25), the positive bias for $D_{\mathbf{g}}^1$ and τ^{12} are corrected by 'NC 1' and 'NC 2'. For v^2, the no correction case has a negative bias. 'NC 1' corrected the negative bias in v^2, whereas 'NC 2' produced a positive bias of a similar magnitude compared to the no correction case. For $D_{\mathbf{g}}^2$, the no correction case has a negative bias and both 'NC 1' and 'NC 2' resulted in a positive bias of a similar magnitude compared to the no bias case.

4.4. Discussion

Since the current dMRI spatial resolution does not allow one to directly image the complete tissue microstructure, inferring the macroscopic parameters of biological tissues from voxel-level dMRI signals is standard practice. Clearly, the inference quality depends strongly

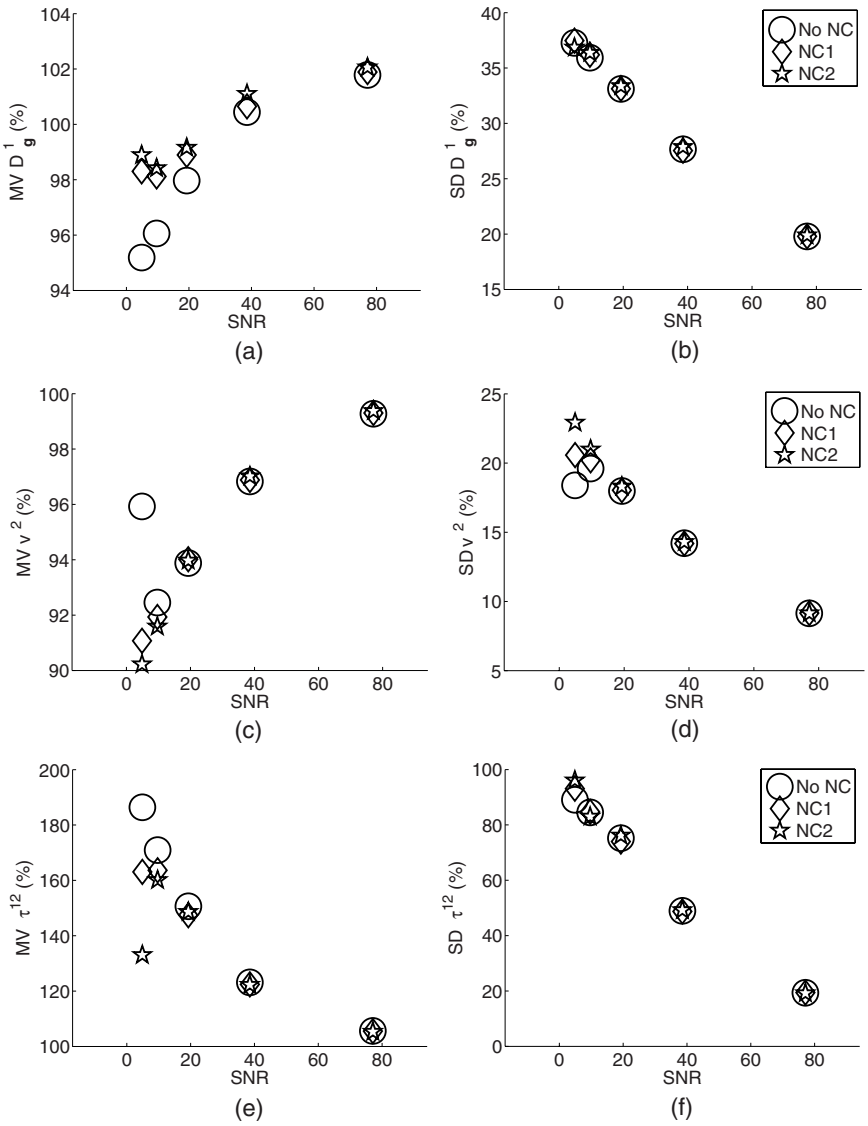

Figure 7. 76-spheres example. Noise correction using Rice distribution. The sequence is $\delta = \Delta = 40$ ms, LS problem uses the full list of 42 b-values in equation (32) and LS weighting $w_k = 1$. The strategies are described in section 4.2. The mean values and standard deviations of the estimated parameters, $D_{\mathbf{g}}{}^1$, v^2, τ^{12}, normalized by their true values, are shown. True parameters are given by equation (29). The SNR of the estimation strategy is defined as the SNR at the lowest b-value. The SNR is defined in equation (38). (*a*) MV $\dfrac{D_{\mathbf{g}}^1}{(D_{\mathbf{g}}^1)_{\text{true}}}$. (*b*) SD $\dfrac{D_{\mathbf{g}}^1}{(D_{\mathbf{g}}^1)_{\text{true}}}$. (*c*) MV $\dfrac{v^2}{v^2_{\text{true}}}$. (*d*) SD $\dfrac{v^2}{v^2_{\text{true}}}$. (*e*) MV $\dfrac{\tau^{12}}{\tau^{12}_{\text{true}}}$. (*f*) SD $\dfrac{\tau^{12}}{\tau^{12}_{\text{true}}}$.

on the chosen macroscopic model. As one moves from simpler to more complicated macroscopic models, careful studies of the quality and sensitivity of the estimated macroscopic

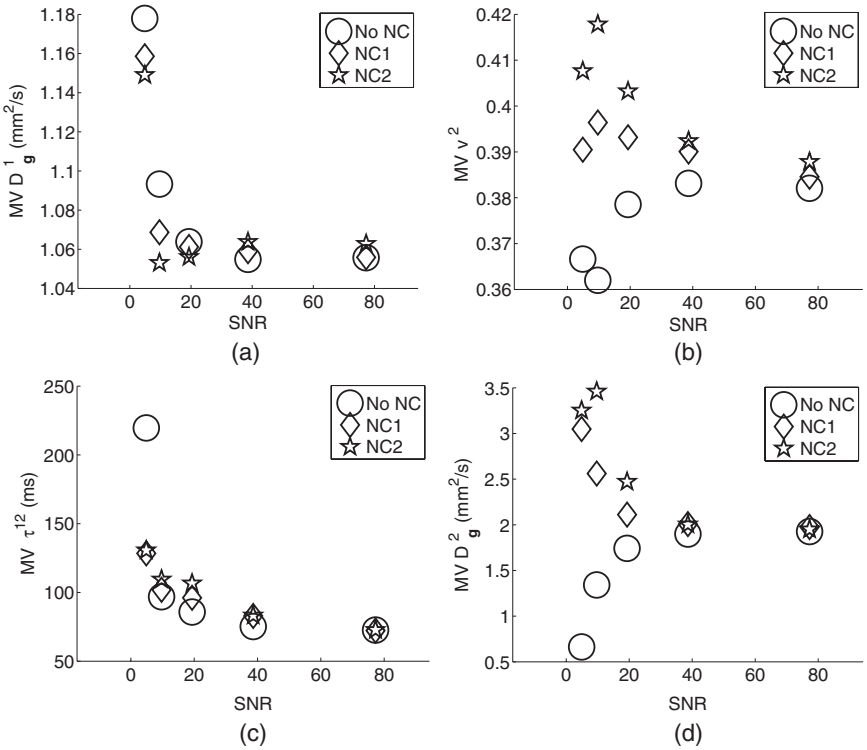

Figure 8. Second example (adapted from *in vivo* data). Noise correction using Rice distribution. The squence is $\delta = 2.5$ ms, $\Delta = 30$ ms, LS problem uses the full list of 42 b-values in equation (32) and LS weighting $w_k = 1$. The strategies are described in section 4.3. The mean values of the estimated parameters, $D_{\mathbf{g}}^1$, v^2, τ^{12}, and $D_{\mathbf{g}}^2$, are shown. The SNR of the estimation strategy is defined as the SNR at the lowest b-value. The SNR is defined in equation (38). (*a*) MV $D_{\mathbf{g}}^1$, (mm^2 s^{-1}). (*b*) MV v^2. (*c*) MV τ^{12} (ms). (*d*) MV $D_{\mathbf{g}}^2$, (mm^2 s^{-1}).

parameters under realistic imaging conditions need to be conducted. Such studies have been conducted for the diffusion tensor model (see, for example, Veraart *et al* (2013b) and Collier *et al* (2014)), as well as the diffusion kurtosis model (see Veraart *et al* (2011) and Veraart *et al* (2013a)). By taking the logarithm of dMRI signal data, both the diffusion tensor and the diffusion kurtosis models become linear in the macroscopic parameters. Linear parameters estimation is inherently easier to solve than its non-linear counterpart and there exist well-developed theory and numerical tools to solve the linear parameters estimation problem. By contrast, the parameters estimation problem associated with some other common macroscopic models, such as the multiple exponential model, the cylindrical neurites model, or the Kärger model, cannot be made linear by a simple transformation of the dMRI signal data. The parameters estimation problem associated with these models remain non-linear. Nevertheless, it is hoped that the additional difficulties in parameters estimation will be justified by other advantages of these macroscopic models, such as better sensitivities to physiological or pathological variations in tissue.

It is in this spirit that we undertake the present study of the FPK model which was derived from the microscopic Bloch–Torrey equation by homogenization techniques. In fact, it is a promising choice for revealing the relation between the macroscopic parameters and the microstructure. The FPK model generalizes the Kärger model (Kärger *et al* 1988) to

non-narrow pulses and the Kärger model has already been used to invert for model parameters from dMRI signals (Stanisz *et al* 1997, Waldeck *et al* 1997, Pfeuffer *et al* 1998, Lee and Springer 2003, Meier *et al* 2003, Quirk *et al* 2003, Roth *et al* 2008, Aslund *et al* 2009, Nilsson *et al* 2009).

We used two sets of data. The first set came from the solution of the Bloch–Torrey equation on a microstructure containing 76 spheres of variable radii. We checked that this solution can be accurately approximated by the FPK model. For numerical convenience, the synthetic signal generated by the FPK model was used. The second set of data came from the *in vivo* rat cortex data (Pyatigorskaya *et al* 2014). These data were shown to be accurately approximated by the bi-exponential model. Once again, we used the simpler representation by the bi-exponential model just for numerical purposes. We showed that these data can as well be accurately approximated by the FPK model.

The synthetic dMRI signals were then corrupted by adding Gaussian noise to their real and imaginary parts. This numerical procedure models the way that the experimental signal gets noisy and yields the Rician noise, as expected. Fitting the noisy signal by weighted least squares method to the FPK signal allows one to estimate the macroscopic parameters of this model. Our goal was to quantify how the quality of the parameters estimation depends on the noise level, sequence timing, weighting coefficients and the range of b-values. In what follows, we discuss the main conclusions of this study.

(a) The mean values of the two estimated parameters $D_{\mathbf{g}}{}^1$ and v^2 remain close to their true values and weakly depend on the noise level (or SNR), see figures 5(a) and (c). The PGSE sequence with shorter pulses ($\Delta = \delta = 25$ ms instead of $\Delta = \delta = 40$ ms) yields a slightly better estimation. In turn, the third parameter τ^{12} exhibits a strong bias from its true value (figure 5(e)), ranging from 10% at the smallest noise (SNR $\simeq$ 80) to 85% at the highest noise (SNR $\approx$ 5). This observation suggests that the FPK signal weakly depends on τ^{12} so that even small noise can significantly affect the inference quality.

(b) There is almost no difference between the standard LS method (with identical weights $w_k = 1$) and the LS method weighted by the inverse of variances of the signal ($w_k = 1/\mathrm{var}\{S_{\sigma,\,i}(b_k)\}$). In general, the correction by variances assigns smaller weights to more noisy points and thus improves the overall quality of the LS fit. In the case of Rician noise, the variance of the noisy signal weakly depends on b-values (section 3.2) and thus has no impact on the estimation quality. We conclude that the standard LS method can be employed. Fitting the signal over a shorter range of b-values also has a weak effect.

(c) The standard deviations of all estimated parameters (or, equivalently, the relative errors as they are plotted in figures 5(b), (d) and (f)), decrease with the SNR, as expected. However, their values remain significant even at the smallest noise level. For instance, the relative errors vary between 20% and 40% for $D_{\mathbf{g}}{}^1$, 8% and 20% for v^2 and 20% and 120% for τ^{12}. As expected, the worst estimation occurs for the residence time τ^{12}, re-affirming our suggestion about the weak dependence of the FPK signal on this parameter. The PGSE with shorter diffusion time yields smaller standard deviations of $D_{\mathbf{g}}{}^1$, v^2 and essentially the same standard deviation of τ^{12}. We also note that the variations between mean values of the estimated parameters among different estimation strategies (figures 5(a), (c) and (e)) are below standard deviations. For this reason, we conclude that all considered estimation strategies are of comparable quality, though the shorter diffusion time can yield a slight improvement.

(d) When the noise level is high, the mean noisy signal deviates significantly from the (noiseless) FPK signal $S(b)$ that was used for the above parameters estimation (figure 2). In other words, fitting noisy signals by $S(b)$ could bias the estimated parameters. In order

to correct for this bias, we replaced the noiseless signal $S(b)$ from the FPK model by the mean noisy signal $\langle S_{\sigma,i}(b)\rangle$. Under the assumption of Rician noise, one can write $\langle S_{\sigma,i}(b)\rangle = \sigma F(S(b)/\sigma)$, with the explicit formula (34) for the function $F(x)$. We compared three estimation strategies: use of noiseless signal $S(b)$, use of bias-corrected signal $\sigma F(S(b)/\sigma)$ with known noise level σ and use of bias-corrected signal $\sigma F(S(b)/\sigma)$ with unknown noise level σ which is added to fitting parameters. We showed that the use of the bias-corrected signal improves the estimation of the worst parameter τ^{12} at the highest noise level (figure 7(*c*)). Another advantage of this scheme is a possibility to estimate the noise level directly from the noisy signal. However, the standard deviations of all three parameters remain almost unchanged (figures 7(*b*), (*d*) and (*f*)). We conclude that the use of bias-corrected signal may be advantageous but it does not allow to reduce standard deviations (i.e. uncertainty range of estimated parameters).

(e) Similar analysis was performed on the second set of data coming from the *in vivo* rat cortex. Since the true values of the macroscopic parameters of the FPK model are not known in this case, it is more difficult to assess the quality of parameters estimation. Our goal here was just to illustrate a potiential application of the parameters estimation on experimental data (figure 6). The mean values of the estimated $D_{\mathbf{g}}^1$ are similar for all 4 strategies, its standard deviations are higher when using smaller b-values (figures 6(*a*) and (*b*)) than the other three strategies. The quality of the estimated v^2 is similar among the 4 strategies (figures 6(*c*) and (*d*)). The mean values of the estimated τ^{12} are different and the standard deviations are higher when using the shorter diffusion time compared to the other 3 strategies (figures 6(*e*) and (*f*)), leading us to conclude that the longer diffusion time should be used. The quality of the estimated $D_{\mathbf{g}}^2$ is the best when using the smaller b-values (figures 6(*g*) and (*h*)). As earlier, the worst estimated parameter is the transfer time τ^{12}, for which the standard deviation is comparable to the mean value. The next worst is $D_{\mathbf{g}}^2$. The other parameters, $D_{\mathbf{g}}^1$ and v^2, can be estimated more accurately.

Although the quality of the parameters estimation remains modest, the FPK model can be considered as a promising tool for inferring the macroscopic parameters of a biological tissue. The worst estimated parameter is the transfer time between the tissue compartments, which is related to the membrane permeability and the surface-to-volume ratios of both compartments. Other parameters (volume fractions and effective diffusivities) can be estimated more accurately. The major advantage of this macroscopic model as compared to other popular choices (such as bi-exponential or kurtosis models) is the fact that the FPK model was derived from the microscopic Bloch–Torrey equation. In other words, the FPK model remains related to the microstructure and can potentially be used to reveal structural features. As a pespective, one can try to optimize the PGSE sequence in order to improve the quality of estimation.

In this paper, we have only estimated the effective diffusion coefficient in a single gradient direction, while it is known that the dMRI signal in brain tissue depends on gradient direction. This dependence is likely to have an impact on the parameters estimation results. For some preliminary results on determining the gradient direction dependence in an anisotropic diffusion geometrical configuration consisting of spheres and cylinders embedded in extracellular space, we refer the readers to the PhD thesis (Nguyen 2014). However, as we have shown in this paper, solving for 4 or 5 macroscopic model parameters accurately is already quite difficult. We believe that estimating the full diffusion tensor, rather than just an effective diffusion coefficient in a single gradient direction, is too challenging for real biological systems at this point.

5. Conclusions

We studied the weighted least squares problem associated with estimating tissue parameters such as the cellular volume fraction, the exchange time and the effective diffusion coefficients using the FPK model of the voxel-level dMRI signal. We found that while the diffusivity in the extracellular compartment and the cellular volume fraction can be estimated relatively accurately, it is quite difficult to obtain accurate estimates of the exchange time between the compartments, especially in the presence of significant noise. We found that noise correction strategies using a Rice signal model improved the parameters estimation only slightly.

Acknowledgments

This work was funded in part by the Agence Nationale de la Recherche project 'SIMUDMRI'.

References

Ababneh Z, Beloeil H, Berde C B, Gambarota G, Maier S E and Mulkern R V 2005 Biexponential parameterization of diffusion and t2 relaxation decay curves in a rat muscle edema model: decay curve components and water compartments *Magn. Reson. Med.* **54** 524–31

Aslund I, Nowacka A, Nilsson M and Topgaard D 2009 Filter-exchange PGSE NMR determination of cell membrane permeability *J. Magn. Reson.* **200** 291–5

Assaf Y, Blumenfeld-Katzir T, Yovel Y and Basser P J 2008 Axcaliber: a method for measuring axon diameter distribution from diffusion MRI *Magn. Reson. Med.* **59** 1347–54

Basser P, Mattiello J and LeBihan D 1994 MR diffusion tensor spectroscopy and imaging *Biophys. J.* **66** 259–67

Bensoussan A, Lions J L and Papanicolaou G 1978 *Asymptotic Analysis for Periodic Structures Studies in Mathematics and Its Applications* vol 5) (Amsterdam North-Holland)

Chabert S, Molko N, Cointepas Y, Le Roux P and Le Bihan D 2005 Diffusion tensor imaging of the human optic nerve using a non-CPMG fast spin echo sequence *J. Magn. Reson. Imag.* **22** 307–10

Chin C L, Wehrli F W, Hwang S N, Takahashi M and Hackney D B 2002 Biexponential diffusion attenuation in the rat spinal cord: computer simulations based on anatomic images of axonal architecture *Magn. Reson. Med.* **47** 455–60

Clark C A and Le Bihan D 2000 Water diffusion compartmentation and anisotropy at high *b* values in the human brain *Magn. Reson. Med.* **44** 852–9

Coatléven J, Haddar H and Li J R 2014 A macroscopic model including membrane exchange for diffusion MRI *SIAM J. Appl. Math.* **74** 516–46

Collier Q, Veraart J, Jeurissen B, den Dekker A J and Sijbers J 2014 Iterative reweighted linear least squares for accurate, fast and robust estimation of diffusion magnetic resonance parameters *Magn. Reson. Med.* accepted (doi: 10.1002/mrm.25351)

Fieremans E, Novikov D S, Jensen J H and Helpern J A 2010 Monte Carlo study of a two-compartment exchange model of diffusion *NMR Biomed.* **23** 711–24

Grebenkov D S 2010 Pulsed-gradient spin-echo monitoring of restricted diffusion in multilayered structures *J. Magn. Reson.* **205** 181–95

Grebenkov D 2007 NMR survey of reflected brownian motion *Rev. Mod. Phys.* **79** 1077–137

Gudbjartsson H and Patz S 1995 The Rician distribution of noisy MRI data *Magn. Reson. Med.* **34** 910–4

Iima M, Yano K, Kataoka M, Umehana M, Murata K, Kanao S, Togashi K and Le Bihan D 2015 Quantitative non-gaussian diffusion and intravoxel incoherent motion magnetic resonance imaging: differentiation of malignant and benign breast lesions *Invest. Radiol.* **50** 205–11

Jensen J H, Helpern J A, Ramani A, Lu H and Kaczynski K 2005 Diffusional kurtosis imaging: the quantification of non-gaussian water diffusion by means of magnetic resonance imaging *Magn. Reson. Med.* **53** 1432–40

Jespersen S N, Kroenke C D, Astergaard L, Ackerman J J and Yablonskiy D A 2007 Modeling dendrite density from magnetic resonance diffusion measurements *NeuroImage* **34** 1473–86

Kärger J, Pfeifer H and Heinik W 1988 Principles and application of self-diffusion measurements by nuclear magnetic resonance *Adv. Magn. Reson.* **12** 1–89
Lee J H and Springer C S 2003 Effects of equilibrium exchange on diffusion-weighted NMR signals: the diffusigraphic shutter-speed? *Magn. Reson. Med.* **49** 450–8
Li J R, Nguyen H T, Van Nguyen D, Haddar H, Coatleven J and Le Bihan D 2014 Numerical study of a macroscopic finite pulse model of the diffusion MRI signal *J. Magn. Reson.* **248** 54–65
Meier C, Dreher W and Leibfritz D 2003 Diffusion in compartmental systems. I. A comparison of an analytical model with simulations *Magn. Reson. Med.* **50** 500–9
Mulkern R V *et al* 1999 Multi-component apparent diffusion coefficients in human brain *NMR Biomed.* **12** 51–62
Nguyen D V, Li J R, Grebenkov D and Le Bihan D 2014 A finite elements method to solve the Bloch–Torrey equation applied to diffusion magnetic resonance imaging *J. Comput. Phys.* **263** 283–302
Nguyen H T 2014 Numerical investigations of some mathematical models of the diffusion MRI signal *PhD Thesis* (University of Paris-11, France)
Niendorf T, Dijkhuizen R M, Norris D G, van Lookeren Campagne M and Nicolay K 1996 Biexponential diffusion attenuation in various states of brain tissue: implications for diffusion-weighted imaging *Magn. Reson. Med.* **36** 847–57
Nilsson M, Alerstam E, Wirestam R, Stahlberg F, Brockstedt S and Latt J 2010 Evaluating the accuracy and precision of a two-compartment Karger model using monte carlo simulations *J. Magn. Reson.* **206** 59–67
Nilsson M, Latt J, Nordh E, Wirestam R, Stahlberg F and Brockstedt S 2009 On the effects of a varied diffusion time *in vivo* : Is the diffusion in white matter restricted? *Magn. Reson. Imag.* **27** 176–87
Pfeuffer J, Flogel U, Dreher W and Leibfritz D 1998 Restricted diffusion and exchange of intracellular water: theoretical modelling and diffusion time dependence of 1H NMR measurements on perfused glial cells *NMR Biomed.* **11** 19–31
Pyatigorskaya N, Le Bihan D, Reynaud O and Ciobanu L 2014 Relationship between the diffusion time and the diffusion MRI signal observed at 17.2 tesla in the healthy rat brain cortex *Magn. Reson. Med.* **72** 492–500
Quirk J D, Bretthorst G L, Duong T Q, Snyder A Z, Springer C S, Ackerman J J and Neil J J 2003 Equilibrium water exchange between the intra- and extra-cellular spaces of mammalian brain *Magn. Reson. Med.* **50** 493–9
Rice S O 1944 Mathematical analysis of random noise *Bell Syst. Tech. J.* **23** 282–332
Roth Y, Ocherashvilli A, Daniels D, Ruizcabello J, Maier S, Orenstein A and Mardor Y 2008 Quantification of water compartmentation in cell suspensions by diffusion-weighted and T2-weighted MRI *Magn. Reson. Imag.* **26** 88–102
Schwarcz A, Bogner P, Meric P, Correze J L, Berente Z, Pál J, Gallyas F, Doczi T, Gillet B and Beloeil J C 2004 The existence of biexponential signal decay in magnetic resonance diffusion-weighted imaging appears to be independent of compartmentalization *Magn. Reson. Med.* **51** 278–85
Sen P N and Basser P J 2005 A model for diffusion in white matter in the brain *Biophys. J.* **89** 2927–38
Sijbers J, den Dekker A, Scheunders P and Van Dyck D 1998 Maximum-likelihood estimation of rician distribution parameters *IEEE Trans. Med. Imaging* **17** 357–61
Stanisz G J, Wright G A, Henkelman R M and Szafer A 1997 An analytical model of restricted diffusion in bovine optic nerve *Magn. Reson. Med.* **37** 103–11
Stanisz G J 2003 Diffusion MR in biological systems: tissue compartments and exchange *Isr. J. Chem.* **43** 33–44
Torrey H 1956 Bloch equations with diffusion terms *Phys. Rev.* **104** 563–5
Veraart J, Rajan J, Peeters R R, Leemans A, Sunaert S and Sijbers J 2013a Comprehensive framework for accurate diffusion MRI parameter estimation *Magn. Reson. Med.* **70** 972–84
Veraart J, Sijbers J, Sunaert S, Leemans A and Jeurissen B 2013b Weighted linear least squares estimation of diffusion MRI parameters: strengths, limitations and pitfalls *NeuroImage* **81** 335–46
Veraart J, Van Hecke W and Sijbers J 2011 Constrained maximum likelihood estimation of the diffusion kurtosis tensor using a Rician noise model *Magn. Reson. Med.* **66** 678–86
Waldeck A, Kuchel P W, Lennon A J and Chapman B E 1997 NMR diffusion measurements to characterise membrane transport and solute binding *Prog. Nucl. Magn. Reson. Spectrosc.* **30** 39–68
Xu J, Does M and Gore J 2007 Numerical study of water diffusion in biological tissues using an improved finite difference method *Phys. Med. Biol.* **52** N111–26